Macedonian Journal of Chemistry and Chemical Engineering, Vol. **45**, No. 1, pp. xx–xx (2026)

MJCCA9 – ISSN 1857-5552
e-ISSN 1857-5625
Received: January 3, 2026 DOI: 10.20450/mjcce.2026.3405
Accepted: May 8, 2026 *Original scientific paper*

COMPUTATIONAL INSIGHTS INTO PFOS AND PFOA ENCAPSULATION WITHIN A COVALENT "CAGE-OF-CAGES" ARCHITECTURE

Avni Berisha

Department of Chemistry, Faculty of Mathematics and Natural Sciences, University of Prishtina, Prishtina, Kosovo

avni.berisha@uni-pr.edu

The widespread contamination of water by per- and polyfluoroalkyl substances (PFAS) demands the development of efficient and selective removal strategies. In this study, we use computational methods to investigate the potential of a covalently bonded "cage-of-cages" molecular architecture for PFAS sequestration, employing density functional theory (DFT), molecular dynamics (MD), nudged elastic band (NEB) calculations, and noncovalent interaction (NCI) analyses. DFT calculations show stronger binding of perfluorooctanesulfonic acid (PFOS) (–33.07 kcal/mol) relative to perfluorooctanoic acid (PFOA) (−24.63 kcal/mol), primarily driven by van der Waals and electrostatic interactions within the confined cage interior. MD simulations confirm the stable confinement of both PFAS molecules in water, while NEB calculations reveal a higher relative desorption energy barrier for PFOS (109.18 kcal/mol) compared with PFOA (99.84 kcal/mol), implying stronger retention of PFOS within the cage cavity. Collectively, these findings demonstrate that hierarchical molecular cages served as promising supramolecular platforms for PFAS sequestration, offering a mechanistic computational basis for future experimental validation and rational adsorbent design.

Keywords: molecular cage; polyfluoroalkyl substances (PFAS) adsorption, density functional theory (DFT); nudged elastic band (NEB); quantum theory of atoms in molecules (QTAIM)

КОМПЈУТЕРСКИ СОГЛЕДУВАЊА ЗА ЕНКАПСУЛАЦИЈАТА НА PFOS И PFOA ВО КОВАЛЕНТНА „КАФЕЗ-ОД-КАФЕЗИ“ АРХИТЕКТУРА

Широкораспространетото загадување на водата со пер- и полифлуороалкилни супстанци (PFAS) бара развој на ефикасни и селективни стратегии за нивно отстранување. Во оваа студија се користени компјутерски методи за да се испита потенцијалот на ковалентно поврзана молекуларна архитектура „кафез-од-кафези“ за издвојување на PFAS, применувајќи теорија на функционалот на електронската густина (DFT), молекулска динамика (MD), пресметки со методот метод на еластична лента (NEB) и анализи на нековалентни интеракции (NCI). DFT пресметките покажуваат посилно врзување на перфлуорооктансулфонска киселина (PFOS) (–33,07 kcal/mol) во споредба со перфлуорооктанска киселина (PFOA) (−24,63 kcal/mol), главно поттикнато од вандервалсовски и електростатски интеракции во ограничената внатрешност на кафезот. MD симулациите потврдуваат стабилно задржување на двете PFAS молекули во вода, додека NEB пресметките откриваат повисока релативна енергетска бариера за десорпција кај PFOS (109,18 kcal/mol) во споредба со PFOA (99,84 kcal/mol), што укажува на посилно задржување на PFOS во шуплината на кафезот. Севкупно, овие резултати покажуваат дека хиерархиските молекуларни кафези претставуваат ветувачки супрамолекуларни платформи за издвојување на PFAS, нудејќи механистичка компјутерска основа за идни експериментални валидации и рационален дизајн на адсорбенти.

Клучни зборови: молекуларен кафез; адсорпција на полифлуороалкилни супстанци (PFAS); теорија на функционал на густина (DFT); метод на еластична лента (NEB);
квантна теорија на атоми во молекули (QTAIM)

1. INTRODUCTION

Molecular cages constitute an innovative class of materials possessing the remarkable ability to encapsulate guest molecules within their well-defined, hollow structures.[1] Constructed through approaches such as dynamic covalent chemistry, these systems enable the modular assembly of diverse architectures designed for specific functionalities.[2] The primary types of molecular cages include purely organic cages, metal–organic cages (MOCs), and hydrogen-bonded cages, each displaying unique structural features. Their intrinsic porosities and tunable cavities render these cages valuable in applications spanning catalysis, molecular recognition, separation technologies, and drug delivery.[3,4]

A key advantage of molecular cages is their structural flexibility, which enables cooperative diffusion and efficient guest encapsulation.[5] Functioning as molecular flasks, they create confined environments for chemical reactions and shield sensitive molecules from external conditions.[6] Recent advances have incorporated photochromic and luminescent functionalities, extending their applications into optoelectronics and materials science.[7,8] Additionally, hybrid systems combining cages with porous organic frameworks (POFs) or metal nanoparticles (MNPs) have exhibited enhanced stability and functionality, thereby expanding their utility in catalysis, gas separation,[4] and advanced materials synthesis.[3]

Beyond these applications,[9] molecular cages have emerged as promising candidates for environmental remediation, particularly for the removal of per- and polyfluoroalkyl substances (PFAS). PFAS constitute persistent synthetic contaminants associated with hormonal disruption, cancer, and long-term ecological harm.[10] Due to their exceptional stability, resulting from strong C–F bonds, conventional treatment methods prove ineffective. The tunable porosity and selective binding properties of molecular cages render them well-suited for PFAS capture, primarily through electrostatic interactions with the anionic head groups of these pollutants.[11] Recent work has shown that adaptive organic cages and metallacages effectively capture perfluorinated acids from aqueous solutions, demonstrating the strong potential of these systems for water purification.[11] For example, a porous adaptive metallacage displayed exceptional adsorption efficiency for perfluorinated carboxylic acids (PFCAs) in simulated water contamination scenarios. These findings underscore the potential of molecular cages as advanced adsorbents by utilizing their structural features for enhanced capture performance.

Tailored design plays a pivotal role in optimizing interactions between molecular cages and PFAS. Positively charged sites within cage structures strengthen electrostatic attraction to the anionic head groups of PFAS, thereby significantly improving adsorption efficiency.[12] This effect is particularly crucial because the charge distribution of PFAS molecules critically influences their removal efficacy. Electrostatic interactions between the charged cage sites and the negatively charged PFAS head groups facilitate effective capture mechanisms.[13]

The size and shape of molecular cages can be tailored to enhance selective PFAS recognition via cavity matching, electrostatic attraction, hydrophobic confinement, and dispersion-rich contacts.[14] Studies have demonstrated that molecular cages and related supramolecular adsorbents[15] effectively capture diverse PFAS-based species, ranging from long-chain perfluorinated acids to emerging contaminants like GenX.[13] Nevertheless, while these results demonstrate the promise of cage-based PFAS capture, key challenges persist, including practical scalability, regeneration, and performance in complex water matrices, all of which require further investigation.[10,16]

Current PFAS-based adsorbents encompass carbon-based materials, ion-exchange resins, polymeric sorbents, cyclodextrin-based networks, metal–organic frameworks (MOFs), and molecular cages.[10,16,17] Carbon-based adsorbents see widespread use due to their availability, high surface area, and hydrophobic adsorption capacity, but their selectivity often declines in complex water matrices containing natural organic matter and competing contaminants.[10,17] Ion-exchange and polymeric adsorbents offer stronger electrostatic interactions with anionic PFAS head groups, yet regeneration, fouling, and variable uptake across structurally diverse PFAS present significant limitations.[13,16,17] Cyclodextrin-based polymers feature defined hydrophobic cavities and they leverage cooperative hydrophobic and electrostatic interactions.[20,21] MOFs exhibit tunable porosity, high surface area, and adjustable metal nodes or organic linkers; however, their long-term water stability and scalability vary substantially with framework structure.[18,19] In contrast, molecular cages possess discrete and well-defined internal cavities that enable design for size/shape complementarity, electrostatic recognition, hydrophobic confinement, and dispersion-rich host–guest contacts.[2,11,15,23]

Despite these advances, most reported studies either focus on experimental adsorption performance or on specific host–guest binding models. Comprehensive multiscale computational descriptions of PFOS and PFOA confinement within hierarchical covalent cage architectures are still lacking. Specifically, the interplay of cage free volume, size compatibility, dispersion interactions, polar head-group contacts, dynamic aqueous stability, and desorption resistance has yet to be fully elucidated for covalently bonded cage-of-cages systems. Bridging this gap could yield molecular-level insights that inform rational design of next-generation supramolecular adsorbents for PFAS sequestration.

Here, we computationally investigate the interaction of two representative and widely studied PFAS-based compounds,[22] namely PFOS and PFOA, within the cavity of a covalently bonded cage-of-cages molecular architecture[23] (Scheme 1).

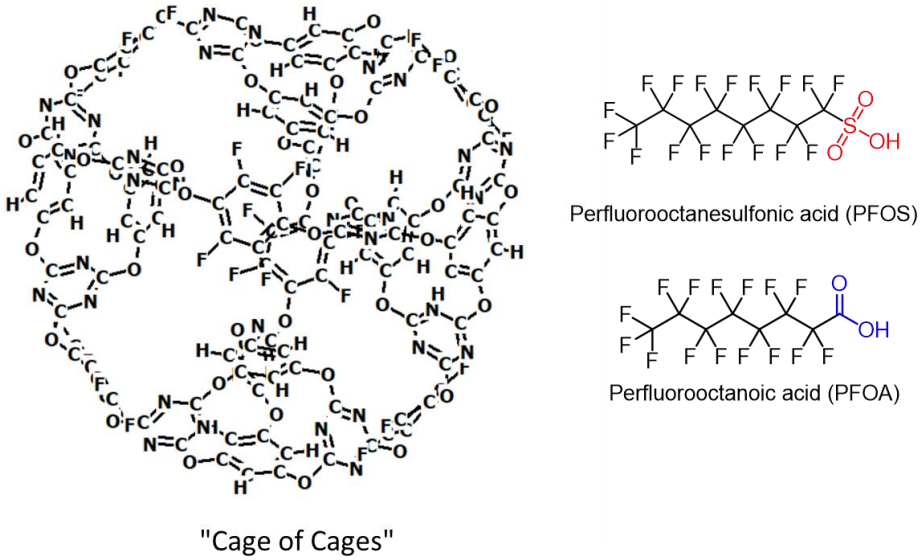

Scheme 1. Schematic of the covalently bonded cage-of-cages architecture (left) and the two representative per- and polyfluoroalkyl substances (PFAS) examined in this study: perfluorooctanesulfonic acid (PFOS, upper right) and perfluorooctanoic acid (PFOA, lower right). Key functional groups are color-coded: red (sulfonic) and blue (carboxylic).

By combining volumetric analysis, DFT interaction energies, Reduced Density Gradient (RDG)/non-covalent interaction (NCI) visualization, QTAIM analysis, MD simulations, NEB calculations, and Hirshfeld surface/energy framework analysis, this study offers a molecular-level understanding of how structural confinement and non-covalent interactions control PFAS retention within the cage cavity. In this initial investigation, we employed the crystal structure of the molecular cage, available from the Cambridge Crystallographic Data Centre (CCDC deposition number 2303319).[24]

2. COMPUTATIONAL METHODOLOGY

2.1. *Volume determination*

To ensure accurate and reliable results, we analyzed the molecular cage's structural and volumetric properties using a combination of computational tools. The cage's initial structure, retrieved from the Cambridge Crystallographic Data Centre (CCDC deposition number 2303319), underwent optimization first with MOPAC to obtain an energetically minimized geometry, followed by density functional theory (DFT) calculations (as detailed in the Methodology section).

The optimized structure underwent analysis using MoloVol[25] (version 1.1.1) to calculate key volumetric parameters, including van der Waals volume, probe-occupied volume, probe-accessible volume, and free volume. MoloVol implemented a grid-based approach with a two-probe system (small probe radius: 1.2 Å; large probe radius: 20 Å) to evaluate molecular accessibility and locate cavities within the cage. A grid resolution of 0.2 Å was specified, and atom-specific radii were assigned as follows: O (1.5 Å), H (1.2 Å), N (1.66 Å), F (1.46 Å), and C (1.77 Å). The analysis determined a free volume of 1469.45 Å^3 (Fig. 1), corresponding to the space available for guest molecule encapsulation.

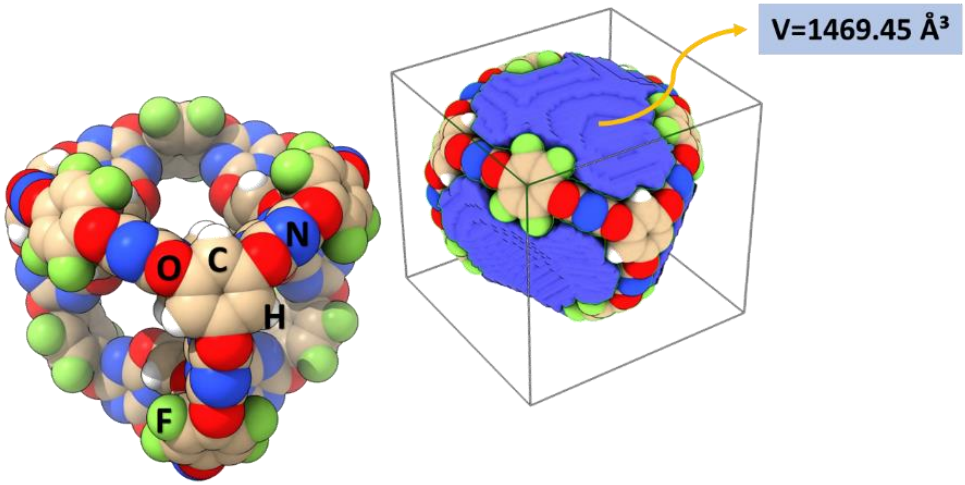

Fig. 1. Optimized structure of the covalently bonded cage-of-cages molecular architecture and its calculated internal cavity/free volume using MoloVol analysis. The volume assessment enabled evaluation of whether the molecular cage could geometrically accommodate PFOS and PFOA as guest molecules.

Surface maps generated during the analysis were visualized using ChimeraX,[26] allowing for detailed examination of van der Waals surfaces, molecular surfaces, and cavity distributions. This comprehensive approach provided precise characterization of the molecular cage's structural properties, demonstrating its potential suitability for PFAS-based encapsulation studies.

Single-probe calculations (probe radius: 1.2 Å) were performed to calculate the molecular volumes of PFOS and PFOA, which were found to be 296.968 Å^3 and 250.248 Å^3, respectively. Based on the cage's cavity volume, combined with shape compatibility, noncovalent interactions (hydrogen bonding, van der Waals forces, and electrostatic effects), and host flexibility that enabled cavity adaptation to guest dimensions, the analysis confirmed that the cage could effectively accommodate these PFAS-based molecules.

2.2. *Density functional theory (DFT)*

All quantum chemical calculations were performed using the ORCA 6.0 software package.[27–29]

Conformer Search and Starting Geometries – Prior to DFT optimization, a conformational search was conducted for the molecular cage, PFOS, and PFOA to obtain reliable starting geometries. The search utilized the GFN2-xTB Hamiltonian in XTB (version 6.4.0) with the global optimization algorithm (GOAT) for molecules and clusters of atoms, systematically explored torsional degrees of freedom and generated approximately 500 conformers per molecule. Conformers within 5 kcal/mol of the global minimum were selected, and the lowest-energy structures underwent re-optimization at the ωB97M-D4/def2-SVP level with the conductor-like polarizable continuum model (CPCM) solvation (water). Guest–host complexes were subsequently constructed using the XTB DOCKER module, which sampled both interior and exterior orientations, and all resulting structures were refined at the DFT level prior to subsequent analyses.

Geometry optimizations were performed using the wB97M-D4 functional,[30] a state-of-the-art range-separated hybrid functional optimized for accurate modeling of systems governed by noncovalent interactions.[31] The def2-SVP basis set[32] was used for all atoms, achieving an optimal balance between computational efficiency and accuracy. This double-ζ basis set proved particularly effective for organic molecules and medium-sized systems, delivering reliable predictions while maintaining reasonable computational costs.

To incorporate solvation effects, the CPCM was implemented with waster as the solvent.[33,34] This approach models solute–solvent interactions by representing the solvent as a continuous dielectric medium. The CPCM improved the accuracy of computed structural and energetic properties by accounting for the stabilizing effects of the aqueous environment.

All structural optimizations were conducted in the solvated phase, with strict convergence criteria for energy, gradient, and displacement applied. Unless noted otherwise, tight convergence settings were employed to guarantee precision. Calculations were accelerated through parallelization, with 128 processors utilized.[35] This computational protocol, combining the wB97M-D4 functional, def2-SVP basis set, and CPCM solvation model, established a robust framework for investigating molec-

ular interactions, yielding reliable predictions of structural and energetic properties under realistic conditions. Reduced density gradient (RDG) and non-covalent interaction (NCI) analyses were carried out using the Multiwfn[36,37] and visual molecular dynamics (VMD) software packages.[38]

2.3. *Nudged elastic band (NEB) calculations*

The transition states (TS) for the studied reactions were located and characterized using the DMol^3 module in Materials Studio. The calculations implemented the linear synchronous transit/quadratic synchronous transit (LST/QST) method with parameters specifically optimized for accuracy and efficiency.[39] A maximum of 20 conjugate gradient steps and two QST cycles were employed, with a gradient tolerance set at 0.020 Å.

Stringent self-consistent field (SCF) convergence criteria were applied, including a density convergence of 1.0×10^{-5} Ha, charge mixing of 0.2, spin mixing of 0.5, and a direct inversion of the iterative subspace (DIIS) Pulay scheme over six iterations, permitting up to 9,999 total SCF cycles. Electronic structure calculations utilized an unrestricted spin polarization approach with a neutral charge. The double numerical basis set with d-functions (DND) was chosen, along with the Minnesota 11-L (M11L) exchange-correlation functional. A global cutoff of 3.6 Å was set for all calculations. The computational results yielded energy profiles, optimized TS geometries, and vibrational frequency analyses to verify the nature of the transition states.

Nudged elastic band (NEB) calculations were conducted to map the desorption pathways of PFOS and PFOA from the cage cavity and to determine relative desorption barriers along the selected reaction coordinate. All NEB pathway calculations were performed in Materials Studio using the DMol^3 module at the M11-L/DND level of theory. This hybrid computational approach was selected because the ωB97M-D4/def2-SVP/CPCM protocol employed for ORCA geometry optimizations and interaction-energy calculations was not directly compatible with NEB pathway calculations within Materials Studio.

To maintain consistency between the two computational stages, the starting host–guest geometries for NEB calculations were derived from the ωB97M-D4/def2-SVP-optimized structures. Thus, the NEB calculations served primarily to assess the relative desorption resistance of PFOS and PFOA rather than to predict absolute experimental desorption energies. While the use of different computational levels may influence the quantitative magnitude of the barriers, the qualitative PFOS > PFOA retention trend remained consistent with the DFT interaction energies and non-covalent interaction analyses.

2.4. *Molecular dynamics (MD) simulations*

Molecular dynamic simulations were conducted using the Forcite module in Materials Studio (version 2020) with the COMPASSIII force field[40] and force-field-assigned charges. The cage-PFAS complexes were placed in an explicit cubic water box, and initial velocities were randomly assigned. All simulations were performed in the canonical (NVT) ensemble at 298 K, with temperature regulated by a Berendsen thermostat (decay constant: 0.1 ps). Newton's equations of motion were integrated using a 1.0 fs timestep, and each trajectory was extended for 5.0 ns, (5,000,000 simulation steps). This 5.0 ns simulation duration was chosen to enable an initial short-timescale host–guest stability and confinement in explicit water while ensuring computational feasibility for the large solvated cage–PFAS-based systems.

Since longer simulations would offer more extensive conformational sampling, the MD results were interpreted as evidence of short-timescale dynamic stability rather than exhaustive long-timescale adsorption behavior. Long-range electrostatic interactions were calculated using an atom-based summation with cubic spline truncation (cutoff distance: 15.5 Å; spline width: 1.0 Å; buffer width: 0.5 Å). The same cutoff scheme was applied to van der Waals interactions. Throughout each trajectory, structural stability and PFAS-based confinement within the cage were assessed by monitoring total energy, potential energy, kinetic energy distribution, and radius of gyration (R_g).

The computational workflow employed multiple theoretical models, each chosen for its specific application. The ωB97M-D4/def2-SVP/CPCM level was selected to characterize optimized host–guest structures and interaction energies, while the DMol^3/M11-L/DND approach was applied to NEB pathway calculations. Additionally, the COMPASSIII force field was utilized to evaluate dynamic stability in explicit water. This multilevel approach enabled the acquisition of complementary information at a computationally feasible cost for the large supramolecular system.

However, absolute values derived from different levels of theory should not be directly compared without appropriate caution. Consequently, the primary conclusions were drawn from consistent qualitative trends across methods, notably the stronger binding, higher relative desorption resistance, and more stable aqueous confinement observed for PFOS relative to PFOA.

3. RESULTS

2.5. *Density functional theory (DFT)*

Accurate determination of interaction energies in supramolecular host–guest systems proved essential for elucidating their binding affinities and stability. In this study (Fig. 2), the interaction energies of PFOS and PFOA within the molecular cage were computed both with and without dispersion energy contributions. The findings demonstrated a significant influence of dispersion forces on the overall interaction energies.

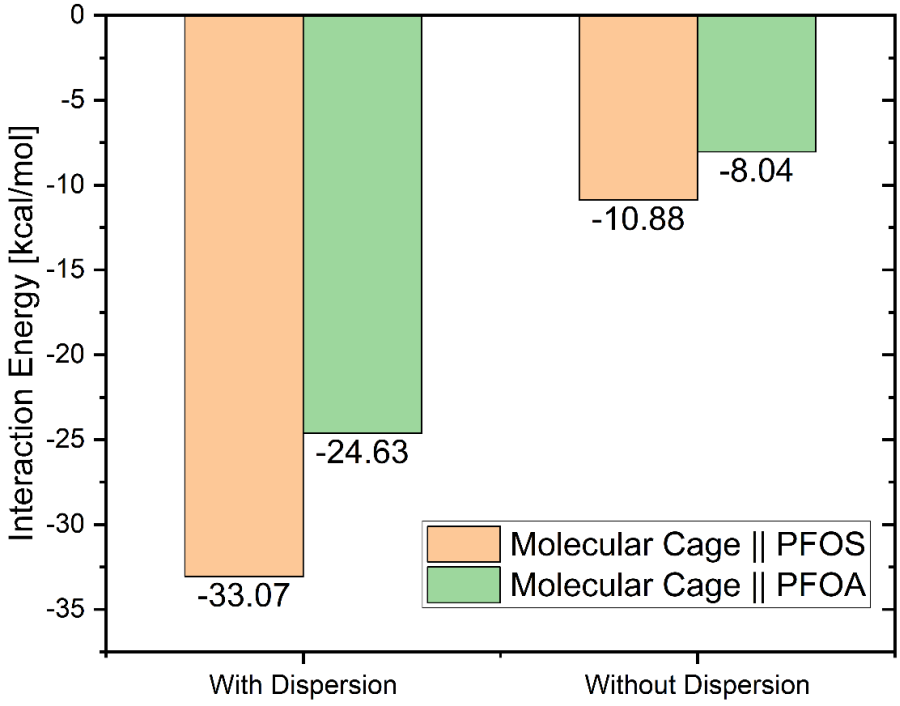

Fig. 2. DFT-calculated interaction energies between the molecular cage and the encapsulated PFOS/PFOA molecules, determined with and without D4 dispersion correction. This comparison revealed the predominant role of London dispersion interactions in stabilizing host–guest complexes, demonstrating stronger overall binding for PFOS relative to PFOA.

When dispersion corrections were applied, the interaction energy of the molecular cage with PFOS measured –33.07 kcal/mol, whereas for PFOA, it measured –24.63 kcal/mol. However, excluding dispersion effects resulted in a substantial reduction of interaction energies to –10.88 kcal/mol and –8.04 kcal/mol for PFOS and PFOA, respectively.

For PFOS, van der Waals interactions contributed 67.10% to the total interaction energy within the molecular cage, indicating their dominant role in system stabilization. Conversely, for PFOA, van der Waals interactions comprised only 32.63% of the total interaction energy, indicating a more significant contribution from other intermolecular forces, particularly electrostatic interactions. This display underscored the distinct interaction profiles of PFOS and PFOA within the molecular cage, likely attributable to differences in molecular structure, polarity, or spatial accommodation within the cage environment.

This pronounced energy shift highlighted the critical need to account for dispersion interactions in density functional theory (DFT) calculations.[41] The use of a dispersion-corrected functional or the incorporation of dispersion correction in DFT proved essential for accurately modeling these interactions, as many standard functionals do not inherently include long-range dispersion effects.[41,42]

These findings underscored the critical need for dispersion-inclusive computational methods, including DFT-D4, when investigating weak interactions in supramolecular chemistry. Omission of dispersion corrections risks producing misleading conclusions about molecular interactions, especially in systems where noncovalent forces govern complex stability. Additionally, to further elucidate the interaction mechanisms, the DFT-derived parameters were calculated, and a correlation matrix plot of the computed values was generated (Fig. 3) for comprehensive analysis.

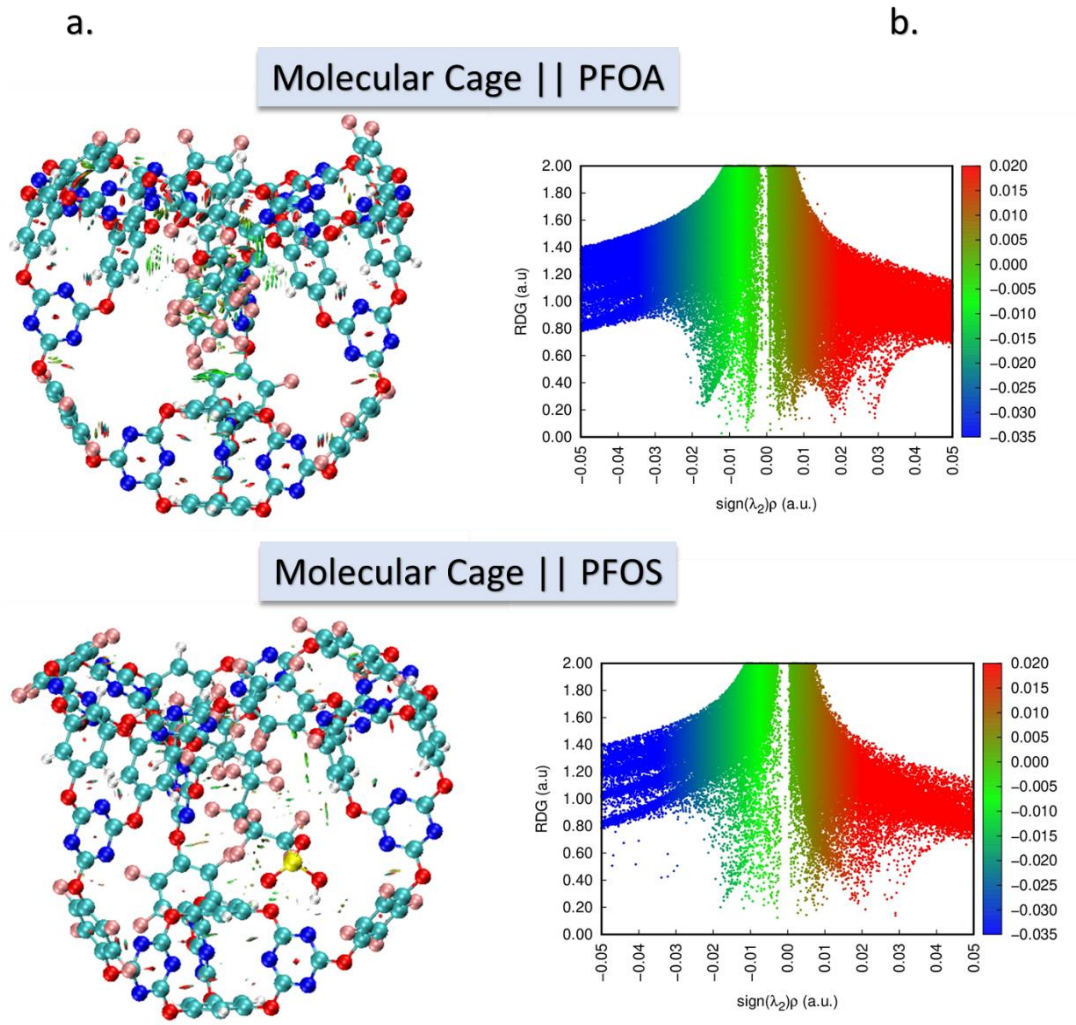

Fig. 3. a. Noncovalent interaction (NCI) isosurface maps and b. Reduced density gradient (RDG) scatter plots for PFOS and PFOA encapsulated within the cage-of-cages cavity. The RDG/NCI analysis was performed to visualize weak host–guest interactions. Blue regions indicate strongly attractive interactions, green regions represent van der Waals contacts, and red regions correspond to steric repulsion. The extensive green isosurfaces demonstrate that dispersion-dominated contacts between the fluorinated PFAS-based chains and the cage interior constituted stabilization contributors.

Reduced density gradient/noncovalent interaction (RDG/NCI) analysis[43] was performed to visualize and classify the noncovalent host–guest interactions responsible for PFOS and PFOA stabilization within the cage cavity. In the RDG scatter plots, negative values of sign(λ_2)ρ corresponded to attractive interactions, near-zero regions were associated primarily with van der Waals contacts, and positive values indicated steric repulsion. The corresponding NCI isosurfaces revealed that both PFAS-based molecules were stabilized predominantly by extensive green regions, demonstrating dispersion-dominated contacts between the fluorinated chains and the cage interior, along with additional localized attractive interactions involving the polar head groups.

The correlation analysis between interaction energy and various DFT-derived parameters[45,46] (Fig. 4) offered insights into how electronic and intermolecular forces affected the stability of PFAS-based molecules within molecular cages. Among the observed trends, dispersion energy exhibited the strongest positive correlation with interaction energy (r = 0.90). This correlation demonstrated that van der Waals forces played a dominant role in stabilizing these complexes, making significant contributions to their overall binding energy. Thus, dispersion interactions emerged as the primary driving force behind the interactions between the molecular cage and PFAS-based molecules.

A strong positive correlation was also found between interaction energy and lowest unoccupied molecular orbital (LUMO) energy (r = 0.73), indicating that molecules with higher LUMO energy tended to form stronger interactions. This relationship suggested the influence of electron affinity on molecular stability, since higher LUMO energy corresponds to greater electron-accepting ability.

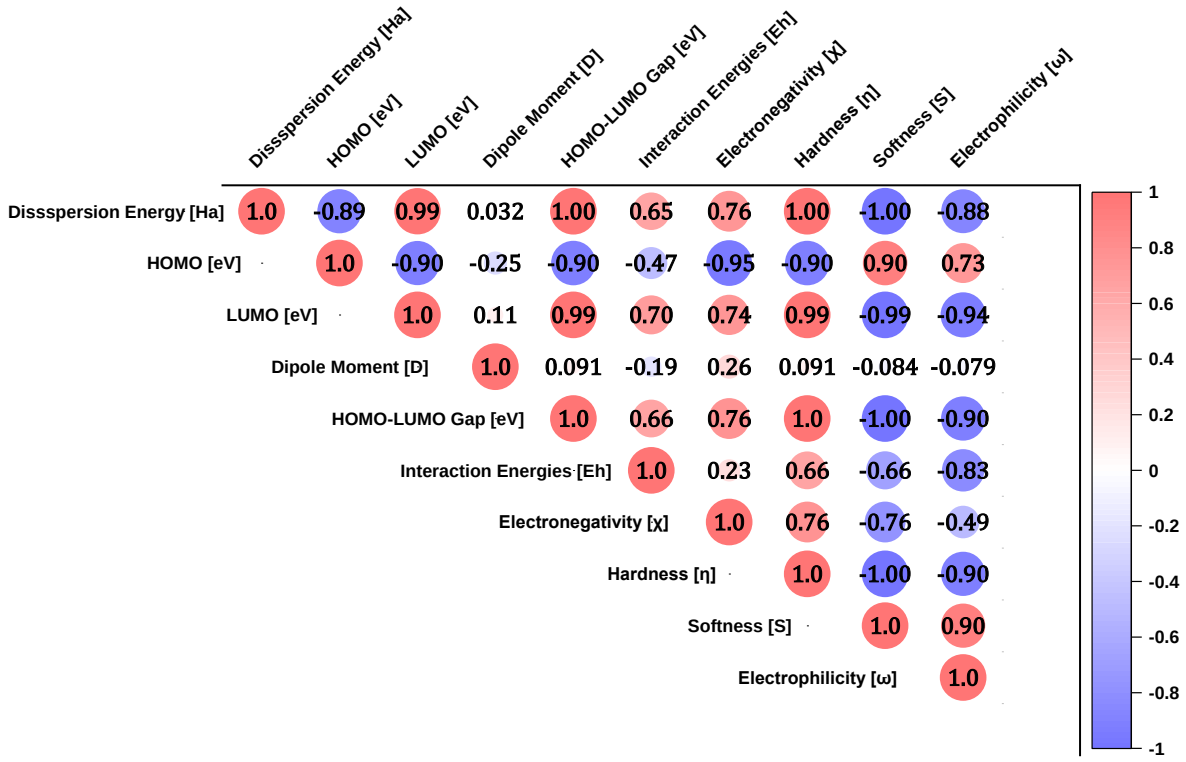

Fig. 4. Descriptor comparison matrix illustrating the qualitative relationship between interaction energy and selected DFT-derived electronic parameters for PFOS and PFOA within the molecular cage. Since only two representative PFAS molecules were investigated, the matrix was intended as a qualitative descriptor comparison rather than a statistically robust correlation analysis.

Similarly, the highest occupied molecular orbital (HOMO)–LUMO gap (r = 0.83), which reflects electronic stability, exhibited a strong correlation with interaction energy. This relationship suggested that molecules with wider HOMO–LUMO gap tended to form stronger intermolecular interactions, thereby reinforcing the role of electronic structure in determining stability. Conversely, HOMO energy showed a moderate correlation (r = 0.31), indicating that while the donor orbital energy contributed to interaction energy, its influence was less pronounced than other factors.

Notably, the dipole moment displayed a weak negative correlation (r = –0.29), suggesting that higher molecular polarity might slightly decrease interaction energy. This observation implied that highly polar molecules interacted differently within the cage compared with nonpolar molecules, potentially due to competing electrostatic effects.

Overall, the analysis revealed that dispersion interactions served as the primary stabilizing force in these systems, while frontier molecular orbital properties, particularly LUMO energy and the HOMO–LUMO gap, also played critical roles. The weak negative correlation of the dipole moment with interaction energy further confirmed that electrostatic effects were not the primary drivers of stability in these molecular interactions.

From a design standpoint, these RDG/NCI indicated that future PFAS-based-binding cages should incorporate three key structural features: a cavity sufficiently large to accommodate long-chain PFAS-based molecules, dispersion-rich inner surfaces designed of maximizing contact with fluorinated chains, and strategically positioned polar or charged sites capable of interacting with sulfonate or carboxylate head groups. The stronger interaction observed for PFOS suggested that increasing fluorinated-chain contact area and optimizing head-group recognition could serve as effective strategies for enhancing PFAS selectivity and retention in next-generation molecular cage adsorbents.

2.6. *Nudged elastic band (NEB) calculations*

The transition state (TS) calculations (Fig. 5) for the desorption of perfluorooctanoic acid (PFOA) and perfluorooctane sulfonic acid (PFOS) from the molecular cage yielded key insights into their relative stability, binding strength, and release mechanisms. Both PFAS-based molecules demonstrated strong confinement within the cage, as evidenced by their high energy barriers, although differences in their desorption profiles revealed varia-

tions in their interactions with the host system. The computed energy barrier (E_a) for PFOS was 109.18 kcal/mol, while PFOA showed a slightly lower barrier of 99.84 kcal/mol.

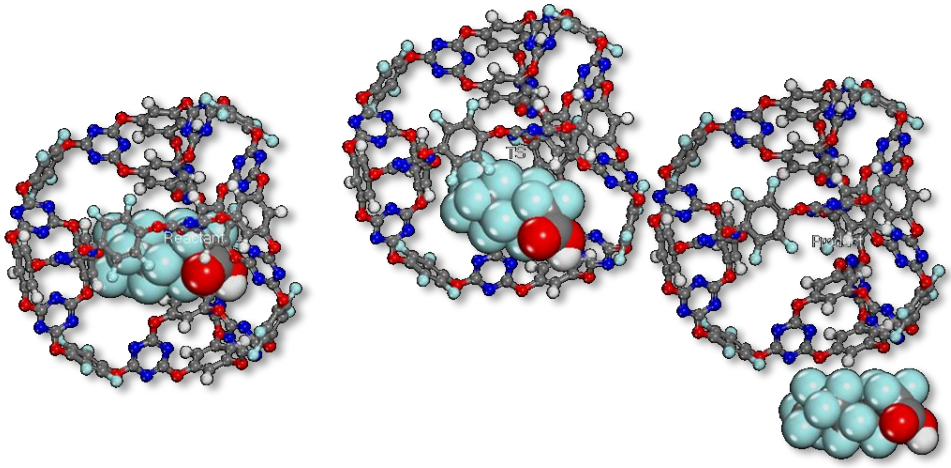

Fig. 5. Representative nudged elastic band (NEB) desorption pathway illustrating the movement of a PFAS-based molecule from the interior to the exterior of the molecular cage. NEB calculations were performed to determine relative desorption resistance along the defined pathway.

These findings indicated that PFOS experienced stronger confinement within the molecular cage, requiring greater energy input for desorption. The reaction energy (ΔE) was 14.60 kcal/mol for PFOS and 12.63 kcal/mol for PFOA, demonstrating that both molecules were thermodynamically more stable within the cage than in the free state. However, the slightly higher reaction energy for PFOS further confirmed its greater affinity for the host system relative to PFOA.

Despite following an analogous release mechanism, the higher energy barrier of PFOS suggested stronger host–guest interactions, likely influenced by its sulfonic ($–SO_3H$) functional group, which exhibited stronger electrostatic and hydrogen-bonding interactions compared with the carboxylic (–COOH) group of PFOA. Moreover, PFOS's larger molecular size and increased fluorine content may have contributed to enhanced van der Waals interactions, thereby stabilizing it within the cage.

The high energy barriers for both PFOA and PFOS indicated that the molecular cage functioned as an effective sequestration system, significantly reducing the likelihood of spontaneous release into the surrounding environment. However, the lower energy barrier for PFOA implied that it could be more readily removed under controlled conditions, whereas PFOS, with its stronger binding affinity, might require additional external stimuli, such as thermal activation or chemical modification, to facilitate its release.

To further characterize the confinement and desorption behavior of these molecules, rotational time correlation function analysis and electronic structure evaluations could provide deeper insights into their dynamics and interaction mechanisms within the molecular cage.

It is important to note that the calculated desorption barriers were designed to offer relative insight into the confinement strength of PFOS and PFOA within the selected cage model. Since the NEB calculations were conducted using a different computational framework than the DFT optimizations and followed an idealized desorption coordinate, the absolute barrier values could not be interpreted as direct experimental desorption energies. Instead, the comparison between PFOS and PFOA demonstrated that PFOS was more strongly retained under the computational model employed, in agreement with the stronger interaction energy obtained from DFT calculations.

2.7. *PFAS-based molecules stability inside molecular cage assets via MD calculations*

To assess whether PFAS-based molecules retained adsorptive behavior within a molecular cage and whether the cage could effectively host them in a dynamic system at room temperature, a simulation was constructed. This system comprised a molecular cage encapsulating a PFAS molecule within its cavity, solvated by 2,000 water molecules (Fig. 6).

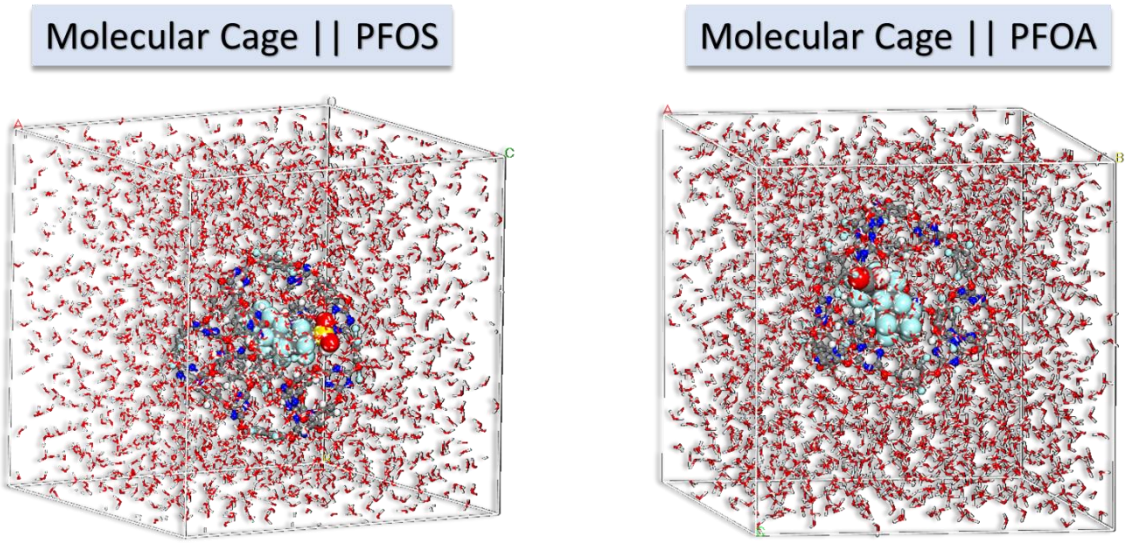

Fig. 6. Molecular dynamics simulation model of the cage–PFAS complex solvated in an explicit water box containing 2,000 water molecules. This solvated system was employed to assess the short-timescale dynamic stability and confinement behavior of PFOS and PFOA within the cage cavity under canonical (NVT) conditions at 298 K.

In the second step, the system was subjected to molecular dynamics (MD) simulation using the COMPASSIII force field to evaluate the structural integrity of the Molecular cage||PFAS system in solution. The simulation was performed in the canonical (NVT) ensemble, with a constant temperature of 298 K maintained by a Berendsen thermostat (decay constant: 0.1 ps). To precisely capture the system's behavior, Newton's equations of motion were integrated using a 0.1 fs time step, ensuring high precision in atomic trajectory tracking. The total simulation duration reached 2,500 ps, enabling comprehensive assessment of the system's stability and interactions over time.

The radius of gyration (Rg) distributions of both PFOA and PFOS within the molecular cage were analyzed to evaluate their structural stability and confinement during the simulation. The results showed that PFOA displayed Rg values ranging from 2.86 Å to 3.56 Å, with a dominant probability density observed in the 3.25–3.45 Å range. Likewise, PFOS exhibited Rg values between 3.83 Å and 4.37 Å, with a peak probability density found in the 4.17–4.23 Å range (Fig. 7).

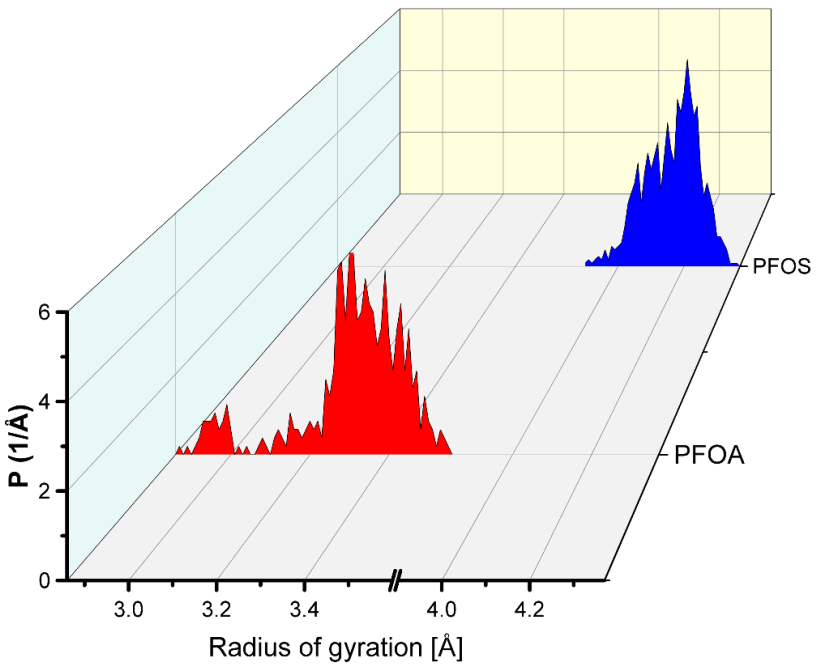

Fig. 7. Probability density distributions of the radius of gyration (R_g) for PFOS and PFOA obtained from molecular dynamics simulations in explicit water.

The relatively narrow distributions observed for both molecules indicated that they maintained structural stability within the molecular cage throughout the simulation. The absence of significant deviations towards lower R_g values (< 2.8 Å for PFOA and < 3.8 Å for PFOS) demonstrated that neither molecule experienced substantial compaction nor collapse, which would otherwise have suggested excessive structural distortion from external forces. Similarly, the lack of persistent higher Rg values (> 3.6 Å for PFOA and > 4.4 Å for PFOS) confirmed that both molecules remained encapsulated, without extending or escaping from the cage environment.

The observed R_g fluctuations represented minor conformational adjustments, likely resulting from intermolecular interactions with the cage and solvent molecules. Nevertheless, these fluctuations did not correspond to trends associated with molecular destabilization or cage escape. The confinement of both PFOA and PFOS appeared to be governed by a combination of van der Waals interactions, hydrogen bonding, hydrophobic effects, and electrostatic forces.

While the MD simulations demonstrated stable encapsulation of both PFAS molecules in an aqueous environment, the current simulations did not explicitly incorporate complex environmental water matrices, competing ions, natural organic matter, pH-dependent speciation, or adsorbent regeneration. Thus, the MD results were interpreted as evidence of molecular-level confinement stability rather than direct proof of practical water-treatment performance.

2.8. *QTAIM analysis of PFOS and PFOA molecules*

The QTAIM analysis (Fig. 8) of the interactions between the molecular cage and the PFOS/PFOA molecules provided a comprehensive understanding of the bonding and interaction mechanisms contributing to their stabilization within the molecular cage framework. This analysis revealed the interplay of covalent-like bonding, hydrogen bonds, and van der Waals forces, elucidating the structural integrity and dynamic stability of these encapsulated systems.

Strong covalent interactions – Covalent interactions were characterized by high electron density ($\rho > 0.29$ a.u. for PFOS and $\rho > 0.25$ a.u. for PFOA) and significantly negative Laplacian ($\nabla^2\rho < -0.39$ a.u.). In the PFOS system, bonds such as C95–O205 ($\rho = 0.2976$ a.u., $\nabla^2\rho = -0.3950$ a.u.) and C34–O220 ($\rho = 0.3074$ a.u., $\nabla^2\rho = -0.3801$ a.u.) displayed negative total energy densities ($H = -0.4736$ a.u., $H = -0.4969$ a.u.) and high bond degrees ($B = 2.26, 2.24$). For PFOA, similar strong interactions were observed, such as the C258–C260 bond ($\rho = 0.2563$ a.u., $\nabla^2\rho = -0.6547$ a.u., $H = -0.2082$ a.u., $B = 5.66$). These bonds constituted the primary stabilization framework for the molecules and exhibited low ellipticity ($\varepsilon < 0.04$), indicating uniform and stable bonding.

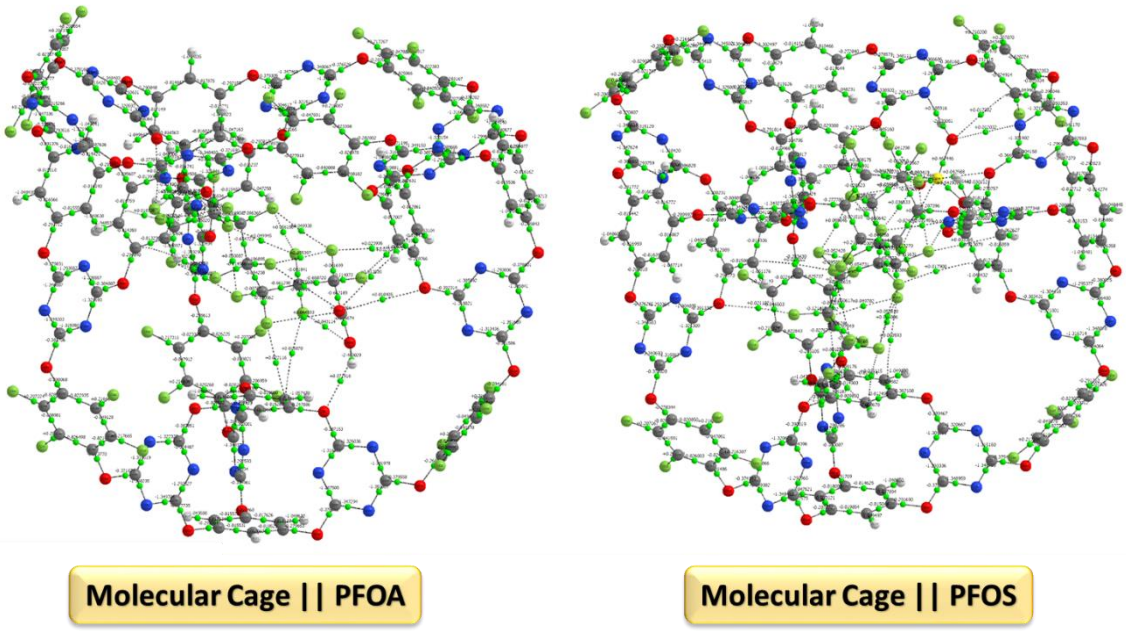

Fig. 8. Quantum theory of atoms in molecules (QTAIM) molecular graphs for PFOA and PFOS encapsulated within the molecular cage, computed at the ωB97M-D4/def2-SVP level of theory.

Hydrogen bonding interactions – In the PFOS molecule, moderate hydrogen bonds contributed to additional stabilization. Notable examples included N100–H270 (ρ = 0.0368 a.u., $\nabla^2\rho$ = 0.1059 a.u., H = –0.2940 a.u., B = 1.45) and H153–O260 (ρ = 0.0061 a.u., $\nabla^2\rho$ = 0.0263 a.u., H = –0.0042 a.u., B = 0.78). These bonds, with moderate ellipticity values ($\varepsilon \approx 0.03$–0.33), indicated slight strain but still provided significant stability. In PFOA, the O8–O257 interaction (ρ = 0.0045 a.u., $\nabla^2\rho$ = 0.0184 a.u., H = 0.0008 a.u., B = 0.78) suggested weaker hydrogen bonding but contributed to the formation of a secondary network of interactions within the cavity.

Weak van der Waals interactions – Both systems exhibited weak van der Waals forces characterized by low electron density ($\rho < 0.01$ a.u.) and positive Laplacian ($\nabla^2\rho > 0$ a.u.). For PFOS, examples included C63–F250 (ρ = 0.0042 a.u., $\nabla^2\rho$ = 0.0170 a.u., H = 0.0009 a.u., |V|/G = 0.72) and O8–F255 (ρ = 0.0037 a.u., $\nabla^2\rho$ = 0.0211 a.u., H = 0.0009 a.u., |V|/G = 0.78). In PFOA, C14–F243 (ρ = 0.0053 a.u., $\nabla^2\rho$ = 0.0221 a.u., H = 0.0010 a.u., B = 0.79) provided weak stabilization.

While individually weak, these interactions collectively played a crucial role in maintaining overall structural stability.

Significant interactions – A particularly notable interaction in the PFOS system was the O259–H270 bond (ρ = 0.3010 a.u., $\nabla^2\rho$ = –2.1331 a.u., H = –0.5929 a.u., |V|/G = 10.94), representing an exceptionally strong hydrogen bond. This interaction was characterized by extremely high stability, minimal bond strain (ε = 0.0121), and uniformity, emphasizing its critical role in anchoring the molecule.

The PFOS and PFOA molecules were stabilized within their respective molecular cages through a synergistic combination of strong covalent bonds, moderate hydrogen bonds, and weak van der Waals forces. Key parameters, including high electron density (ρ), negative total energy density (H), and low ellipticity (ε), collectively ensured effective encapsulation of these molecules. This analysis highlighted the interplay of interaction types, providing a robust framework for the structural integrity of the PFOS- and PFOA-molecular cage systems.

2.9. *Hirshfeld surface analysis, intermolecular interaction energies, and energy frameworks*

Hirshfeld surface analysis enabled an in-depth examination of intermolecular interactions within the crystalline state by focusing on the electron density at molecular contact points.[47–50] This surface, which encloses the molecule, is defined by regions where the electron density from the molecule of interest equals that of its neighboring molecules. Using Crystal Explorer 21.3 software, Hirshfeld surfaces for the studied compounds were generated and analyzed based on parameters including d_e (external distance), d_i (internal distance), d_{norm} (normalized contact distance), shape index, curvedness, and two-dimensional fingerprint plots. Figure 9 presents these Hirshfeld surface maps, displaying the molecule's d_e, d_i, d_{norm}, shape index, and curvedness. Furthermore, fingerprint plots were decomposed to identify specific atom–atom contacts, facilitating the distinction between overlapping interaction types.[51,52] This decomposition provided valuable insights into the relative contributions of various intermolecular contacts, enhancing understanding of the crystal packing arrangement.

The colored regions on the Hirshfeld surfaces in Figure 9 provided valuable insights into diverse molecular surface properties. On the d_{norm} surface, red regions indicated shorter intercontacts, blue regions represented longer ones, and white areas signified contacts close to the van der Waals radii. Red regions corresponded to negative potential with electrophilic tendencies, while blue regions denoted positive potential with nucleophilic characteristics. The shape index, intricately mapped on the surface, revealed red concave regions indicating stacking interactions and blue convex regions representing ring atoms. The varied colors in fragment patches further illustrated different molecular interactions across the surface.

In Figure 10, d_e and d_i represented distances from the Hirshfeld surface to the nearest nuclei outside and inside the surface, respectively. The computed volume within the Hirshfeld surface was 5119.88Å^3, with an area of 2263.96 Å^2.

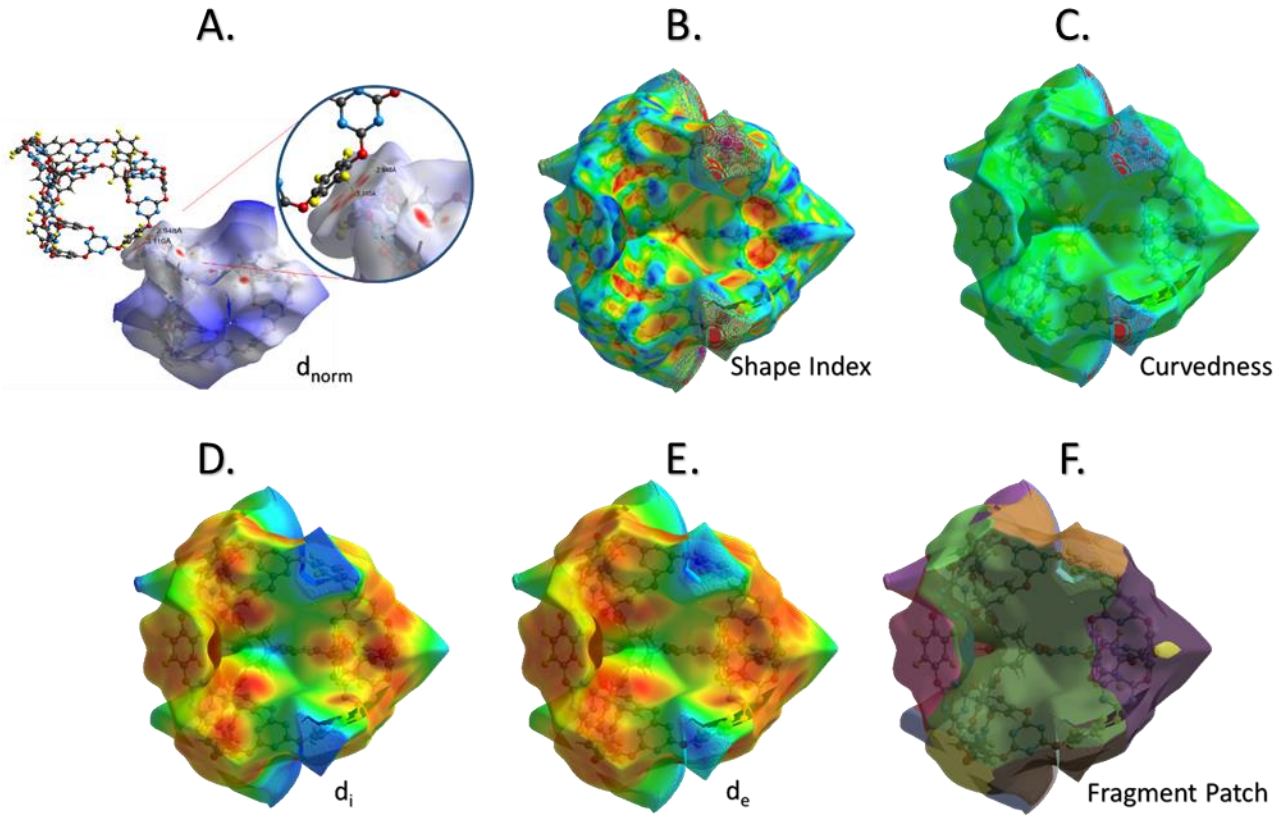

Fig. 9. Hirshfeld surfaces generated using Crystal Explorer 21.3 illustrated molecular interactions: (A) d_{norm} and (B) shape index surfaces revealed H···H interactions, with red and blue triangles (enclosed in a black ellipse) indicating bonding regions. Panels (C–F) show d_e, d_i, and a molecular fragment, providing a detailed view of interaction features.

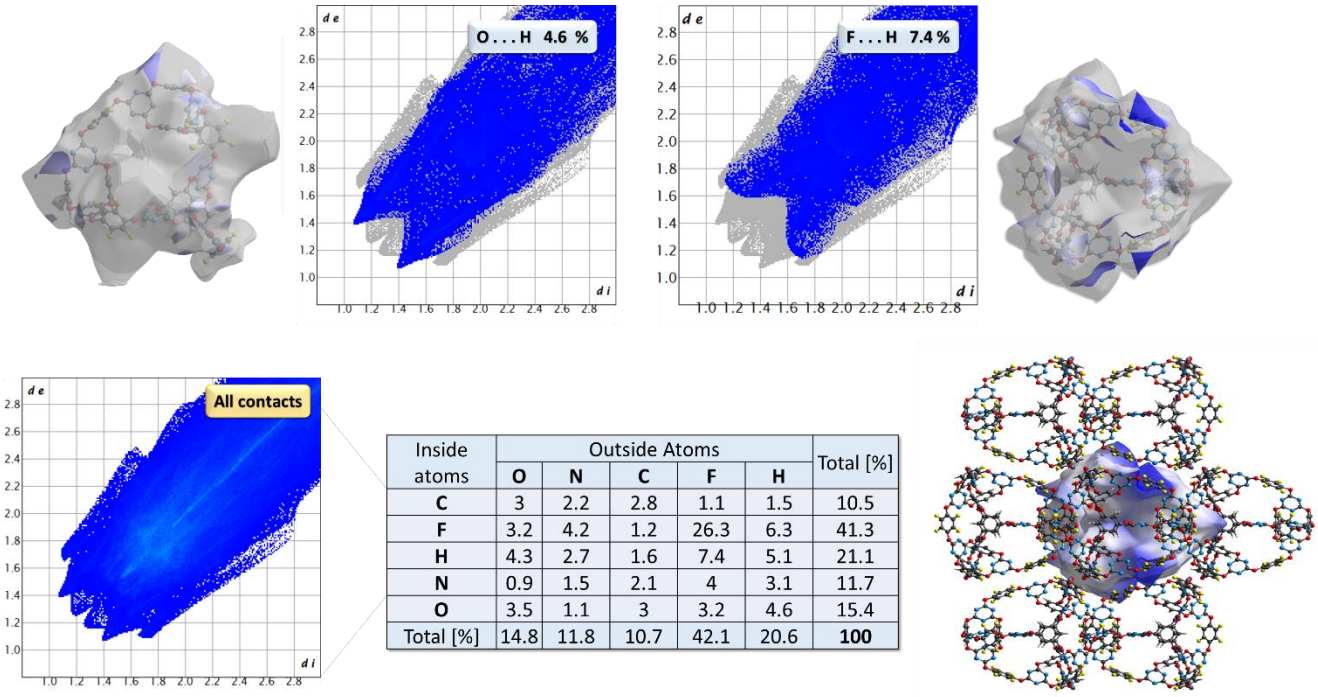

Inside atoms	Outside Atoms					Total [%]
	O	N	C	F	H	
C	3	2.2	2.8	1.1	1.5	10.5
F	3.2	4.2	1.2	26.3	6.3	41.3
H	4.3	2.7	1.6	7.4	5.1	21.1
N	0.9	1.5	2.1	4	3.1	11.7
O	3.5	1.1	3	3.2	4.6	15.4
Total [%]	14.8	11.8	10.7	42.1	20.6	**100**

Fig. 10. Two-dimensional fingerprint plots, three-dimensional Hirshfeld surfaces, and interaction percentage contributions for the encapsulated PFAS–cage system, showing that F···H/H···F and O···H/H···O contacts dominate the host–guest interaction pattern.

The data in Figure 10 provides a breakdown of intermolecular interactions based on atom pairs, expressed as a percentage of total surface contacts. Key observations include:

- Fluorine-related interactions dominated the overall contacts, contributing 41.3%, with significant contributions from F···F (26.3%) and F···H (6.3%) interactions, emphasizing the importance of fluorine in the crystal packing.
- Hydrogen interactions accounted for 21.1%, primarily from H···F (7.4%) and H···H (5.1%), reflecting their substantial presence in the intermolecular contact network.
- Oxygen interactions comprised 15.4%, with O···H (4.6%) being the most prominent, demonstrating oxygen's role in hydrogen bonding and other polar interactions.
- Nitrogen interactions constituted 11.7%, with N···H (3.1%) and N···F (4.0%) as the most significant contributors, highlighting the role of nitrogen in forming polar contacts.
- Carbon-related interactions were the smallest, contributing 10.5%, with C···F (1.1%) and C···C (2.8%) interactions being less significant.
- The total contributions of outside atoms showed that fluorine (42.1%) and hydrogen (20.6%) dominated the intermolecular contact framework, underscoring their central roles in crystal packing stability and molecular interactions.

Visualization of nearest-neighbor energy networks enabled understanding of intermolecular interactions within a molecular crystal. This network is represented using cylinders (Fig. 11), where the width of each cylinder was proportional to interaction strength.[49] For deeper insight, the intermolecular interaction energy was decomposed into four physically meaningful components, each scaled by a specific factor, representing a refinement from the original formulation:

$$E_{tot} = k_{ele}E_{ele} + k_{pol}E_{pol} + k_{dis}E_{dis} + k_{rep}E_{rep}$$

Energy frameworks provided a powerful and intuitive method for visualizing supramolecular arrangements in molecular crystal structures. In these frameworks, cylinders represented molecular packing interactions, with their thickness proportional to interaction strength in various directions. Thicker cylinders indicated stronger interactions, while a uniform scale factor ensured comparability across frameworks by adjusting cylinder sizes consistently.[49,53]

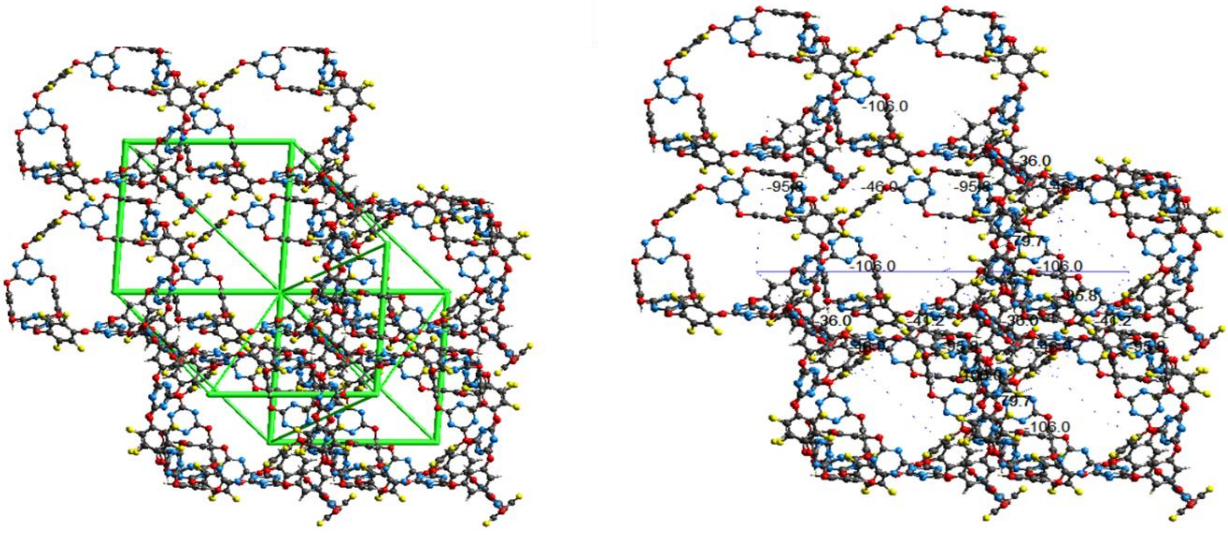

Fig. 11. Energy frameworks visualization for cage-of-cages, showing energy components and total energy interactions.

To maintain visual clarity, weaker interactions below a defined energy threshold were excluded, preventing overcrowding in the representation. The absence of cylinders in a particular direction did not indicate a complete lack of stabilizing interactions but rather reflected a strategic focus on the most significant contributors. This approach emphasized prominent interactions, facilitating clearer and more insightful analysis of the molecular crystal's structural features. [23]

Separate frameworks for electrostatic and dispersion components further refined the analysis, providing valuable insights into the distinct characteristics and contributions of these forces. This method not only enhanced understanding of the crystal's topology but also offered a nuanced perspective on the interplay of forces stabilizing the lattice.[51,53] The interaction energies between the synthesized molecule and its symmetry-related counterparts, calculated using the B3LYP/6-31G(d,p) method, are summarized in Table 1.

T a b l e 1

Interaction energies (kJ/mol) and centroid-to-centroid distances (R, Å) between the molecular cage and its symmetry-related counterparts, computed at the B3LYP/6-31G(d,p) level. The energies were decomposed into electrostatic (E_{ele}), polarization (E_{pol}), dispersion (E_{dis}), repulsion (E_{rep}), and total (E_{tot}) contributions. Positive electrostatic values indicated repulsive interactions

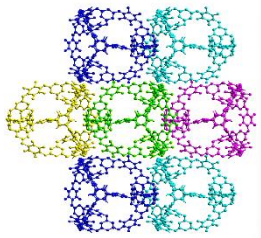	N	Symmetry operator	R	E_{ele}	E_{pol}	E_{dis}	E_{rep}	E_{tot}
	2	–x, y+1/2, –z	21.94	–23.10	–6.50	–57.90	0.00	–79.70
	2	x, y, z	16.29	23.30	–12.90	–139.10	0.00	–106.00
	2	x, y, z	16.58	20.80	–10.20	–126.60	0.00	–95.80
	2	–x, y+1/2, –z	23.64	0.20	–1.00	–40.70	0.00	–36.00
	2	–x, y+1/2, –z	22.83	3.10	–4.90	–46.90	0.00	–41.20
	2	x, y, z	22.47	16.90	–2.60	–71.10	0.00	–46.00

These interactions were characterized by their centroid-to-centroid distances (R, Å) and decomposed into electrostatic (E_{ele}), polarization (E_{pol}), dispersion (E_{dis}), repulsion (E_{rep}), and total energy (E_{tot}) components. Among the interactions, the pair with R = 16.29 Å showed the strongest interaction energy (E_{tot} = –106 kJ/mol), driven predominantly by the dispersion term (E_{dis} = –139.1 kJ/mol), along with a smaller electrostatic contribution (E_{ele} = 23.3 kJ/mol). A comparable interaction was observed at R = 16.58 Å, where E_{tot} = –95.8 kJ/mol, again dominated by dispersion (E_{dis} = –126.6 kJ/mol).

Weaker interactions occurred at longer centroid distances. For instance, the interaction at R = 23.64 Å had a total energy of E_{tot} = –36 kJ/mol, primarily due to dispersion (E_{dis} = –40.7 kJ/mol). Similarly, the interaction at R = 22.83 Å exhibited E_{tot} = –41.2 kJ/mol, with dispersion (E_{dis} = –46.9 kJ/mol) as the most significant component. The interaction at R = 21.94 Å also followed this trend, with E_{tot} = –79.7 kJ/mol, dominated by E_{dis} = –57.9 kJ/mol. The interaction at R = 22.47 Å showed a total energy of E_{tot} = –46 kJ/mol, primarily due to E_{dis} = –71.1 kJ/mol.

These results highlighted the central role of dispersion interactions in stabilizing the molecular crystal, with electrostatic contributions serving as secondary but notable factors in certain interactions. The variation in R and energy components reflected the nuanced interplay of forces governing molecular packing within the crystal lattice.

3. CONCLUSIONS

This study provided a multiscale computational investigation of PFOS and PFOA encapsulation within a covalently bonded hierarchical cage-of-cages molecular architecture. By combining volumetric analysis, DFT calculations, RDG/NCI visualization, QTAIM analysis, NEB calculations, molecular dynamics simulations, and Hirshfeld surface/energy framework analysis, the work elucidated molecular-level insights into the structural, energetic, and dynamic factors governing PFAS confinement within the cage cavity.

Volumetric analysis confirmed that the internal free volume of the cage, calculated at 1469.45 Å^3, was sufficiently large to accommo-

date both PFOS and PFOA, whose molecular volumes were estimated as 296.968 Å^3 and 250.248 Å^3, respectively. This favorable size compatibility supported the host–guest encapsulation. DFT calculations demonstrated that both PFAS molecules interacted favorably with the cage, with PFOS exhibiting stronger interaction energy (–33.07 kcal/mol) than PFOA (–24.63 kcal/mol). Comparison between dispersion-corrected and non-dispersion calculations indicated that London dispersion forces provided a major stabilizing contribution in both complexes, emphasizing the importance of extended perfluoroalkyl chain contacts with the cage interior.

RDG/NCI and QTAIM analyses further supported the predominantly noncovalent nature of PFOS and PFOA stabilization within the cage. The host–guest interaction pattern was governed by a cooperative network of weak-to-moderate attractive contacts, including van der Waals interactions, electrostatic contributions, and localized hydrogen-bonding-type interactions involving the polar head groups. The stronger retention of PFOS was attributable to its larger perfluoroalkyl chain, greater dispersion contact area, and the stronger interaction capacity of the sulfonate group compared with that of the carboxylic group of PFOA.

NEB calculations demonstrated higher relative desorption resistance for PFOS (109.18 kcal/mol) than for PFOA (99.84 kcal/mol), which was consistent with the stronger DFT-calculated interaction energy and more extensive noncovalent contact network observed for PFOS. These barriers were to be interpreted primarily as relative indicators of confinement strength along the selected computational pathway rather than as direct experimental desorption energies. Molecular dynamics simulations in explicit water further indicated that both PFOS and PFOA remained confined within the cage at 298 K over the simulated timescale, with radius-of-gyration distributions showing limited conformational fluctuations and no evidence of collapse or escape. Hirshfeld surface and energy framework analyses additionally confirmed the dispersion-rich character of the cage scaffold and the importance of noncovalent interactions in stabilizing the supramolecular architecture.

The present work demonstrated theoretical and molecular-level evidence that the covalent cage-of-cages scaffold offered a confined, dispersion-rich, and geometrically suitable environment for PFOS and PFOA encapsulation, with PFOS showing stronger calculated binding and greater relative retention than PFOA. However, these findings were to be regarded as computational predictions rather than direct proof of practical water-treatment performance. Experimental adsorption measurements, regeneration and release studies, competitive adsorption tests in the presence of co-contaminants, explicit evaluation of pH and counterion effects, and validation in realistic water matrices will be required to assess the practical applicability of hierarchical molecular cages as selective PFAS remediation materials.

Author Contribution Statement. A.B.: Conceptualization, Methodology, Software, Validation, Formal analysis, Investigation, Data curation, Visualization, writing – original draft, Writing – review & editing, Supervision, Project administration, Funding acquisition.

Data Availability Statement. The data and computational input files supporting the findings of this study are available from the corresponding author (A.B.) upon reasonable request.

REFERENCES

(1) Zhang, L.; Jin, Y.; Tao, G.-H.; Gong, Y.; Hu, Y.; He, L.; Zhang, W. Desymmetrized Vertex Design Toward a Molecular Cage With Unusual Topology. *Angew. Chemie* **2020**. https://doi.org/10.1002/ange.202007454

(2) Montà-González, G.; Sancenón, F.; Martínez-Máñez, R.; Martí-Centelles, V. Purely Covalent Molecular Cages and Containers for Guest Encapsulation. *Chem. Rev.* **2022**, *122* (16), 13636–13708. https://doi.org/10.1021/acs.chemrev.2c00198

(3) Dutta, S. Synthesis and Applications of Cage-Based Covalent Organic Frameworks. *Cryst. Growth & Des.* **2024**. https://doi.org/10.1021/acs.cgd.4c00701

(4) Deegan, M. M.; Bhattacharjee, R.; Caratzoulas, S.; Bloch, E. D. Stabilizing Porosity in Organic Cages Through Coordination Chemistry. *Inorg. Chem.* **2021**. https://doi.org/10.1021/acs.inorgchem.0c03590

(5) Moneypenny, T. P.; Walter, N. P.; Cai, Z.; Miao, Y.; Gray, D. L.; Hinman, J. J.; Lee, S.; Zhang, Y.; Moore, J. S. Impact of Shape Persistence on the Porosity of Molecular Cages. *J. Am. Chem. Soc.* **2017**. https://doi.org/10.1021/jacs.7b00189

(6) Wang, C.; Tian, L.; Wang, Z.; Wang, S.; Gao, N.; Zhou, K.; Yin, X.; Zhang, W.; Zhao, L.; Li, G. Molecular Cage-Bridged Plasmonic Structures With Well-Defined Nanogaps as Well as the Capability of Reversible and Selective Guest Trapping. *Chem. Sci.* **2018**. https://doi.org/10.1039/c7sc03536e

(7) Huang, F. Q.; Ma, L.; Che, Y.; Jiang, H.; Chen, X.; Wang, Y. Corannulene-Based Coordination Cage With Helical Bias. *J. Org. Chem.* **2018**. https://doi.org/10.1021/acs.joc.7b02709

(8) Zou, D.; Li, Z.; Long, D.; Dong, X.; Qu, H.; Yang, L.; Cao, X. Molecular Cage With Dual Outputs of Photochromism and Luminescence Both in Solution and the Solid State. *Acs Appl. Mater. & Interfaces* **2023**. https://doi.org/10.1021/acsami.2c23196

(9) Takezawa, H.; Tabuchi, R.; Sunohara, H.; Fujita, M. Confinement of Water-Soluble Cationic Substrates in a

Cationic Molecular Cage by Capping the Portals With Tripodal Anions. *J. Am. Chem. Soc.* **2020**. https://doi.org/10.1021/jacs.0c08835

(10) Das, S.; Ronen, A. A Review on Removal and Destruction of Per- And Polyfluoroalkyl Substances (PFAS) by Novel Membranes. *Membranes (Basel).* **2022**. https://doi.org/10.3390/membranes12070662

(11) He, Y. Fluorinated Nonporous Adaptive Cages for the Efficient Removal of Perfluorooctanoic Acid From Aqueous Source Phases. *J. Am. Chem. Soc.* **2024**. https://doi.org/10.1021/jacs.3c14213

(12) Kim, J. Evaluation of a Porous Membrane as a Mass-Transfer Efficient Structure for the Adsorption of Per- And Polyfluoroalkyl Substances From Drinking Water. *Acs Es\&t Eng.* **2024**. https://doi.org/10.1021/acsestengg.3c00515

(13) Tan, X.; Dewapriya, P.; Prasad, P.; Chang, Y.; Huang, X.; Wang, Y.; Gong, X.; Hopkins, T. E.; Fu, C.; Thomas, K. V; Peng, H.; Whittaker, A. K.; Zhang, C. Efficient Removal of Perfluorinated Chemicals From Contaminated Water Sources Using Magnetic Fluorinated Polymer Sorbents. *Angew. Chemie* **2022**. https://doi.org/10.1002/anie.202213071

(14) Chaudhary, M. Efficient PFOA Removal From Drinking Water by a Dual-Functional Mixed-Matrix-Composite Nanofiltration Membrane. *NPJ Clean Water* **2023**. https://doi.org/10.1038/s41545-023-00286-2

(15) Camdzic, D. Rapid Capture of Per- And Polyfluoroalkyl Substances Using a Self-Assembling Zirconium-Based Metal-Organic Cage. *Acs Appl. Eng. Mater.* **2023**. https://doi.org/10.1021/acsaenm.3c00592

(16) Chaleshtari, Z. A.; Foudazi, R. A Review on Per- And Polyfluoroalkyl Substances (PFAS) Remediation: Separation Mechanisms and Molecular Interactions. *Acs Es\&t Water* **2022**. https://doi.org/10.1021/acsestwater.2c00271

(17) Zeng, C.; Atkinson, A. J.; Sharma, N.; Ashani, H.; Hjelmstad, A.; Venkatesh, K.; Westerhoff, P. Removing Per- and Polyfluoroalkyl Substances From Groundwaters Using Activated Carbon and Ion Exchange Resin Packed Columns. *Awwa Water Sci.* **2020**. https://doi.org/10.1002/aws2.1172

(18) Li, R.; Alomari, S.; İslamoğlu, T.; Farha, O. K.; Fernando, S.; Thagard, S. M.; Holsen, T. M.; Wriedt, M. Systematic Study on the Removal of Per- And Polyfluoroalkyl Substances From Contaminated Groundwater Using Metal–Organic Frameworks. *Environ. Sci. \& Technol.* **2021**. https://doi.org/10.1021/acs.est.1c03974

(19) Barpaga, D.; Zheng, J.; Han, K. S.; Soltis, J. A.; Shutthanandan, V.; Basuray, S.; McGrail, B. P.; Chatterjee, S.; Motkuri, R. K. Probing the Sorption of Perfluorooctanesulfonate Using Mesoporous Metal–Organic Frameworks From Aqueous Solutions. *Inorg. Chem.* **2019**. https://doi.org/10.1021/acs.inorgchem.9b00380

(20) Xiao, L.; Ching, C.; Ling, Y.; Nasiri, M.; Klemes, M. J.; Reineke, T. M.; Helbling, D. E.; Dichtel, W. R. Cross-Linker Chemistry Determines the Uptake Potential of Perfluorinated Alkyl Substances by B-Cyclodextrin Polymers. *Macromolecules* **2019**. https://doi.org/10.1021/acs.macromol.9b00417

(21) Choudhary, A.; Dong, D.; Tsianou, M.; Alexandridis, P.; Bedrov, D. Adsorption Mechanism of Perfluorooctanoate on Cyclodextrin-Based Polymers: Probing the Synergy of Electrostatic and Hydrophobic Interactions With Molecular Dynamics Simulations. *Acs Mater. Lett.* **2022**. https://doi.org/10.1021/acsmaterialslett.2c00168

(22) Dickman, R. A.; Aga, D. S. A Review of Recent Studies on Toxicity, Sequestration, and Degradation of per- and Polyfluoroalkyl Substances (PFAS). *J. Hazard. Mater.* **2022**, *436*, 129120. https://doi.org/10.1016/J.JHAZMAT.2022.129120

(23) Zhu, Q.; Qu, H.; Avci, G.; Hafizi, R.; Zhao, C.; Day, G. M.; Jelfs, K. E.; Little, M. A.; Cooper, A. I. Computationally Guided Synthesis of a Hierarchical [4[2+3]+6] Porous Organic 'Cage of Cages.' *Nat. Synth. 2024* **2024**, 1–10. https://doi.org/10.1038/s44160-024-00531-7

(24) Groom, C. R.; Bruno, I. J.; Lightfoot, M. P.; Ward, S. C. The Cambridge Structural Database. *urn:issn:2052-5206* **2016**, *72* (2), 171–179. https://doi.org/10.1107/S2052520616003954

(25) Maglic, J. B.; Lavendomme, R. MoloVol: An Easy-to-Use Program for Analyzing Cavities, Volumes and Surface Areas of Chemical Structures. *J. Appl. Crystallogr.* **2022**, *55* (Pt 4), 1033–1044. https://doi.org/10.1107/S1600576722004988/YR5079SUP1.PDF

(26) Meng, E. C.; Goddard, T. D.; Pettersen, E. F.; Couch, G. S.; Pearson, Z. J.; Morris, J. H.; Ferrin, T. E. UCSF ChimeraX: Tools for Structure Building and Analysis. *Protein Sci.* **2023**, *32* (11), e4792. https://doi.org/10.1002/PRO.4792

(27) Neese, F. Software Update: The ORCA Program System—Version 5.0. *Wiley Interdiscip. Rev. Comput. Mol. Sci.* **2022**, e1606. https://doi.org/10.1002/WCMS.1606

(28) Neese, F. Software Update: The ORCA Program System, Version 4.0. *WIREs Comput. Mol. Sci.* **2018**, *8* (1), e1327. https://doi.org/10.1002/wcms.1327

(29) Neese, F.; Wennmohs, F.; Becker, U.; Riplinger, C. The ORCA Quantum Chemistry Program Package. *J. Chem. Phys.* **2020**, *152* (22), 224108. https://doi.org/10.1063/5.0004608/1061982

(30) Mardirossian, N.; Head-Gordon, M. ΩB97M-V: A Combinatorially Optimized, Range-Separated Hybrid, Meta-GGA Density Functional with VV10 Nonlocal Correlation. *J. Chem. Phys.* **2016**, *144* (21). https://doi.org/10.1063/1.4952647

(31) Caldeweyher, E.; Mewes, J. M.; Ehlert, S.; Grimme, S. Extension and Evaluation of the D4 London-Dispersion Model for Periodic Systems. *Phys. Chem. Chem. Phys.* **2020**, *22* (16), 8499–8512. https://doi.org/10.1039/D0CP00502A

(32) Laun, J.; Vilela Oliveira, D.; Bredow, T. Consistent Gaussian Basis Sets of Double- and Triple-Zeta Valence with Polarization Quality of the Fifth Period for Solid-State Calculations. *J. Comput. Chem.* **2018**, *39* (19), 1285–1290. https://doi.org/10.1002/JCC.25195

(33) Garcia-Ratés, M.; Neese, F. Effect of the Solute Cavity on the Solvation Energy and Its Derivatives within the Framework of the Gaussian Charge Scheme. *J. Comput.*

Chem. **2020**, *41* (9), 922–939. https://doi.org/10.1002/JCC.26139

(34) Barone, V.; Cossi, M. Quantum Calculation of Molecular Energies and Energy Gradients in Solution by a Conductor Solvent Model. *J. Phys. Chem. A* **1998**, *102* (11), 1995–2001. https://doi.org/10.1021/JP9716997

(35) Neese, F. The SHARK Integral Generation and Digestion System. *J. Comput. Chem.* **2023**, *44* (3), 381–396. https://doi.org/10.1002/JCC.26942

(36) Lu, T.; Chen, F. Multiwfn: A Multifunctional Wavefunction Analyzer. *J. Comput. Chem.* **2012**, *33* (5), 580–592. https://doi.org/10.1002/jcc.22885

(37) Berisha, A. Unraveling the Electronic Influence and Nature of Covalent Bonding of Aryl and Alkyl Radicals on the B12N12 Nanocage Cluster. *Sci. Reports 2023 131* **2023**, *13* (1), 1–11. https://doi.org/10.1038/s41598-023-28055-8

(38) Humphrey, W.; Dalke, A.; Schulten, K. VMD: Visual Molecular Dynamics. *J. Mol. Graph.* **1996**, *14* (1), 33–38. https://doi.org/10.1016/0263-7855(96)00018-5

(39) Berisha, A. Interactions between the Aryldiazonium Cations and Graphene Oxide: A DFT Study. *J. Chem.* **2019**, *2019*. https://doi.org/10.1155/2019/5126071

(40) Akkermans, R. L. C.; Spenley, N. A.; Robertson, S. H. COMPASS III: Automated Fitting Workflows and Extension to Ionic Liquids. **2020**, *47* (7), 540–551. https://doi.org/10.1080/08927022.2020.1808215

(41) Grimme, S. Supramolecular Binding Thermodynamics by Dispersion-Corrected Density Functional Theory. *Chem. – A Eur. J.* **2012**, *18* (32), 9955–9964. https://doi.org/10.1002/CHEM.201200497

(42) Marom, N.; Tkatchenko, A.; Rossi, M.; Gobre, V. V.; Hod, O.; Scheffler, M.; Kronik, L. Dispersion Interactions with Density-Functional Theory: Benchmarking Semiempirical and Interatomic Pairwise Corrected Density Functionals. *J. Chem. Theory Comput.* **2011**, *7* (12), 3944–3951. https://doi.org/10.1021/CT2005616

(43) Johnson, E. R.; Keinan, S.; Mori-Sánchez, P.; Contreras-García, J.; Cohen, A. J.; Yang, W. Revealing Noncovalent Interactions. *J. Am. Chem. Soc.* **2010**, *132* (18), 6498–6506. https://doi.org/10.1021/JA100936W/SUPPL_FILE/JA100936W_SI_002.PDF

(44) Berisha, A. First Principles Details into the Grafting of Aryl Radicals onto the Free-Standing and Borophene/Ag(1 1 1) Surfaces. *Chem. Phys.* **2021**, *544*, 111124. https://doi.org/10.1016/j.chemphys.2021.111124

(45) Eyupoglu, V.; Akin, M. B.; Kaya, S.; Çaylak, O.; Berisha, A.; Çetinkaya, S. Effective Removal of Methylene Blue Dye from Aqueous Solution Using Macrolepiota Procera Mushroom: Experimental and Theoretical Studies. *J. Mol. Liq.* **2025**, *418*. https://doi.org/10.1016/j.molliq.2024.126714

(46) Gürer, E. S.; Yıldırım, Ş.; Kocyigit, Ü. M.; Berisha, A.; Kaya, S. Experimental, Density Functional Theory, Molecular Docking and ADMET Analyses on the Role of Different Plant Extracts of Aronia Melanocarpa (Michx) Elliot Species on Acetylcholinesterase Enzyme Activity. *J. Mol. Struct.* **2025**, *1321*, 139893. https://doi.org/10.1016/J.MOLSTRUC.2024.139893

(47) McKinnon, J. J.; Jayatilaka, D.; Spackman, M. A. Towards Quantitative Analysis of Intermolecular Interactions with Hirshfeld Surfaces. *Chem. Commun.* **2007**, No. 37, 3814–3816. https://doi.org/10.1039/B704980C

(48) Spackman, M. A.; McKinnon, J. J. Fingerprinting Intermolecular Interactions in Molecular Crystals. *CrystEngComm* **2002**, *4* (66), 378–392. https://doi.org/10.1039/B203191B

(49) Spackman, P. R.; Turner, M. J.; McKinnon, J. J.; Wolff, S. K.; Grimwood, D. J.; Jayatilaka, D.; Spackman, M. A. CrystalExplorer: A Program for Hirshfeld Surface Analysis, Visualization and Quantitative Analysis of Molecular Crystals. *urn:issn:1600-5767* **2021**, *54* (3), 1006–1011. https://doi.org/10.1107/S1600576721002910

(50) Thaçi, V.; Reka, A. A.; Ristovska, N.; Hoti, R.; Berisha, A.; Bogdanov, J. Experimental and Theoretical Studies on (2E,5E)-2,5-Bis(2-Methoxybenzylidene)Cyclopentanone: Structural, Electrochemical, Spectroscopic Features, Solid-State Interactions, Molecular Docking and Adsorption Studies onto 2D Carbon Nanomaterials. *Maced. J. Chem. Chem. Eng.* **2023**, *42* (2), 175-194–175–194. https://doi.org/10.20450/MJCCE.2023.2727

(51) Lee, J. J.; Sobolev, A. N.; Turner, M. J.; Fuller, R. O.; Iversen, B. B.; Koutsantonis, G. A.; Spackman, M. A. Molecular Imprisonment: Host Response to Guest Location, Orientation, and Dynamics in Clathrates of Dianin's Compound. *Cryst. Growth Des.* **2014**, *14* (3), 1296–1306. https://doi.org/10.1021/CG4018129/SUPPL_FILE/CG4018129_SI_002.CIF

(52) Bakheit, A. H.; Abuelizz, H. A.; Al-Salahi, R. Hirshfeld Surface Analysis and Density Functional Theory Calculations of 2-Benzyloxy-1,2,4-Triazolo[1,5-a] Quinazolin-5(4H)-One: A Comprehensive Study on Crystal Structure, Intermolecular Interactions, and Electronic Properties. *Cryst. 2023, Vol. 13, Page 1410* **2023**, *13* (10), 1410. https://doi.org/10.3390/CRYST13101410

(53) Turner, M. J.; Thomas, S. P.; Shi, M. W.; Jayatilaka, D.; Spackman, M. A. Energy Frameworks: Insights into Interaction Anisotropy and the Mechanical Properties of Molecular Crystals. *Chem. Commun.* **2015**, *51* (18), 3735–3738. https://doi.org/10.1039/C4CC09074H.